A Coarse-Grained Model of Oxidized Membranes and Their Interactions with Nanoparticles of Various Degrees of Hydrophobicity

Journal:	*The Journal of Physical Chemistry*
Manuscript ID	jp-2018-119097.R2
Manuscript Type:	Article
Date Submitted by the Author:	02-Mar-2019
Complete List of Authors:	Su, Chanfei; Leibniz-Institut fur Polymerforschung eV, Institute Theory of Polymers Merlitz, Holger; Leibniz-Institut fur Polymerforschung eV Thalmann, Fabrice; ICS-CNRS, Marques, Carlos; ICS-CRM (UP 22 CNRS), Institut Charles Sadron Sommer, Jens-Uwe; Leibniz-Institut fur Polymerforschung eV, Theory of Polymers

SCHOLARONE™
Manuscripts

A Coarse-Grained Model of Oxidized Membranes and Their Interactions with Nanoparticles of Various Degrees of Hydrophobicity

Chan-Fei Su,[†,‡] Holger Merlitz,[†] Fabrice Thalmann,[¶] Carlos Marques,[¶] and Jens-Uwe Sommer[*,†,‡]

†*Leibniz-Institut für Polymerforschung Dresden, 01069 Dresden, Germany*

‡*Technische Universität Dresden, Institute of Theoretical Physics, 01069 Dresden, Germany*

¶*Institut Charles Sadron CNRS UPR 22, 67083 Strasbourg Cedex, France*

E-mail: sommer@ipfdd.de

Abstract

We investigate the consequences of lipid peroxidation on the permeation properties of membranes comprising unsaturated lipid molecules, by means of coarse-grained molecular simulations. After discussion of the impact of peroxidation on the properties of lipid bilayer such as stretching modulus, area per lipid, water permeation, and the distributions of various lipid components across the membrane, we focus in particular on the effect of peroxidation on the passive translocation of small nanoparticles of varying hydrophobicity across lipid bilayers. We consider two types of oxidized lipid bilayers which differ in their degree of peroxidation using a schematic model for the oxidized beads. Consistently with our previous work for non-oxidized lipid bilayers we

find a narrow window of translocation of the nanoparticles when their hydrophobicity is varied. Our studies suggest that oxidized lipid bilayers feature a more hydrophilic environment and strongly enhances the translocation rate of small nanoparticles without formation of pores. Furthermore an optimal permeation rate is found for peroxidized membranes, associated with more hydrophilic nanoparticles than in the case of usual unsaturated lipid bilayers. Strategies for targeting peroxidized lipid membranes in a more specific way are discussed in the light of our findings.

1 Introduction

Biological membranes play a central role in the compartmentalization of cells, the regulation of biochemical exchanges and the signalling pathways[1]. As all living cell components, they are subject to *oxidative stress*, a set of conditions promoting significant changes in their chemical composition. Among the membrane components, mono and polyunsaturated lipids constitute a target for the oxidative processes[2,3]. The mechanisms and consequences of lipid bilayer oxidation are therefore of paramount importance, with implications in the fields of cell aging, cancer and neurodegenerative diseases[4–6].

Lipid alteration caused by reactive oxygen species (ROS) occupies a special place in these studies. Unsaturated lipids are known to confer fluidity to lipid bilayers, and are present in significant proportions in biological membranes. It is established that lipid unsaturated bonds react with singlet oxygen, resulting in the addition of a peroxide group to the carbon chain, along with a shift of the double bond and its *cis* to *trans* conversion. Singlet oxygen production is a natural consequence of the photo excitation of light-absorbing molecules, and is always present when fluorescent markers are present in the system and illuminated[7]. High levels of singlet oxygen creation can be achieved by employing special dyes (such as *e.g.* methylene blue or porphyrins) called photosensitizers. This lies at the basis of photodynamic therapies (PDT), where photo-oxidation is induced for therapeutic purposes[8].

As a consequence of peroxidation, lipid membranes undergo significant structural and

functional modifications[9–12]. Beside displaying lateral expansion and membrane thinning, peroxidized lipid membranes are believed to be more permeable to water, and possibly to a number of other molecular compounds[13,14]. The cause of the enhanced permeation remains to be firmly established, most likely resulting either from a decrease in hydrophobicity of the inner bilayer region, or from the spontaneous formation of membrane pores.

On the other hand, there is also a high interest in understanding the passive translocation mechanisms of small nanoparticles (NPs) across lipid membranes. It is an established fact that NPs with diameters smaller than the thickness of a bilayer are able to cross the layer provided their surface is partial hydrophobic[15]. Recent theoretical investigations suggest that there exists a quite narrow optimum in terms of hydrophobicity, for which the passive permeation coefficient K_{NP} is maximal, though still low compared with light molecular compounds[16–19]. The hydrophobic nature of the NP surface is therefore a key parameter to address when designing devices for drug delivery and cell transfection. A natural question that arises is to determine the extent by which peroxidation changes K_{NP} in terms of magnitude and hydrophobicity dependence.

In this study, we introduce a simple coarse-grained (CG) model of a peroxidized lipid membrane, in order to gain insight into the dependence of K_{NP} with respect to the degree of peroxidation in a lipid bilayer. The lipid molecules are modeled using a simplified version of the Martini model[20,21]. The main properties of the regular, non-oxidized, lipid bilayer model have been presented in[19]. In particular, an hydrophobic scale was set, based on the interpolation between the values for hydrohilic (lipid headgroup, solvent) and hydrophobic (lipid tails) beads of the parameter appearing in the non-bonding truncated Lennard-Jones interaction. The CG lipid molecules were intentionally deprived of electric charges and their topology simplified, to retain only the most essential physical mechanism of bilayer formation, namely the hydrophobic effect. We consider a family of small nanoparticles with variable hydrophobicity which which can be characterized by oil-water partitioning coefficients, see section Details of the Simulation Method.
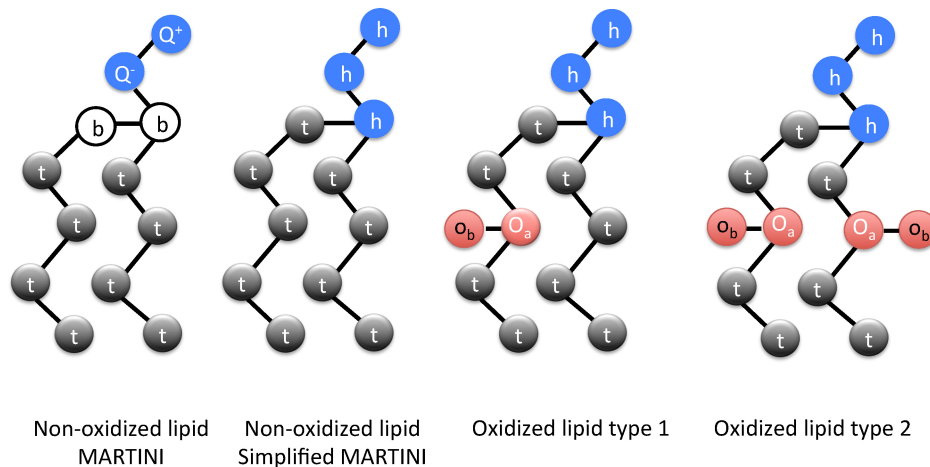
Figure 1: Scheme of the coarse-grained models for non-oxidized lipids[19,20], lipids oxidized on one tail and two tails. Here, Q^+ and Q^- represent the zwitterionic headgroup, and h, t, b, O_a, o_b represent the lipid head, tail, bridge, hydrophobic and hydrophilic oxidized beads respectively.

2 Lipid Models and Simulation Methods

We focus on one special class of compounds: the hydroperoxidized lipid chains, where a peroxide group -OOH is attached to a carbon at the vicinity of the unsaturated double bond C=C. In what follows, the term "oxidized" refers exclusively to this kind of hydroperoxidized lipid. An extension of the modified MARTINI model[19], as sketched in Figure 1, is implemented to construct oxidized lipid bilayers interacting with NPs. In the MARTINI model[20], each non-oxidized group C_4 forming the lipid tail is represented by a hydrophobic bead with a standard size (diameter) of $4.7\mathring{A}$. To reproduce the polar character of the oxidized group C_4OOH that is larger than the original non-oxidized group C_4, a set of hydrophobic beads (representing C_4) with standard size of $4.7\ \mathring{A}$ and hydrophilic beads (representing the -OOH

group) of 4.7 $\mathring{A}$ is introduced, as shown in Figure 1, where hydrophobic oxidized beads are labeled with O_a and hydrophilic oxidized beads with o_b. The adjunction of a hydrophobic oxidized bead to a hydrophilic oxidized bead is chosen to be 3.2 $\mathring{A}$, which is shorter than other bond lengths and was suggested by Thalmann and Guo *et al.*[22], according to systematic investigations and comparisons with experimental studies of hydroperoxidation of 1-palmitoyl-2-oleoyl-sn-glycero-3-phosphocholine (POPC) and 1,2-dioleoyl-sn-glycero-3-phosphocholine (DOPC) bilayers[10] and vesicles[23].

The force field implemented in this work contains a Lennard-Jones (LJ) pair-potential, a bonding potential and an angle potential, as described in Ref[20]. Note that we do not implement an angle potential between oxidized beads and connected tail monomers. Lipid head monomers, solvent beads and hydrophilic oxidized beads are identical in terms of hydrophobic interactions. Moreover, hydrophobic oxidized beads and tail groups are equal in our model. The strategy to mediate effective interaction potentials between NPs of varying hydrophobicities and other components in the systems are described below. The precise meaning of NP hydrophobicity is discussed below, see also Ref[19]. Due to the presence of two different forms of oxidation, two types of oxidized lipids are considered: those oxidized on one and those oxidized on two tails, as shown in Figure 1. Here, oxidized lipid membranes composed of lipids that are oxidized on one tail and two tails are denoted as OX1 and OX2, respectively.

2.1 Details of the Simulation Method

The simulations were conducted with the open source LAMMPS molecular dynamics package[24] using highly parallelized codes. An initial configuration in a cubic box of size $L = 135$ $\mathring{A}$ with 450 oxidized lipid molecules, arranged into two leaflets, and approximately 7900 water beads excluded from the bilayer were equilibrated for 300 ns (10^7 MD steps). The equilibrium process is followed by a production run of 2700 ns ($9 * 10^7$ MD steps), during which a trajectory of 90000 configurations was stored for data analysis. The simulations were

performed in NPT ensembles with time steps of 30 fs, constant temperature of 323 K (damping parameter 3000 fs) with Nose-Hoover thermostat, and constant pressure coupled to a Martyna-Tuckerman-Tobias-Klein (MTTK) barostat[25] (1 bar, damping parameter 30000 fs). The pressure was coupled on x-y direction to minimize the stress of the membrane, while in z coordinate it was not coupled to guaranty a constant solvent pressure. Periodic boundary conditions were implemented in all directions. To study the interactions of NPs and oxidized bilayers OX1 and OX2, 50 and 100 NPs together with 9400 water beads are implemented in the simulations. These correspond to the ratios of NPs to lipids of 1:9 and 2:9, respectively. For comparison, we use results for non-oxidized membranes from our previous work[19].

To obtain the free energy profile of the NPs as a function of their distances to the membrane's midplane, a series of umbrella sampling simulations[26,27] was conducted with the LAMMPS package[24]. In our umbrella sampling simulations, a harmonic bias potential, $U_b = (1/2)K(z - z_0)^2$ with spring constant $K = 0.2$ kcal/(mol$\mathring{A}^2$), was applied to a target position z_0. We recorded the distribution of the particle, $\rho(z)$, during umbrella sampling simulations under the harmonic constraint. An equilibration run of 300 ns (10^7 MD steps) was carried out. It was followed by a production run of 900 ns ($3 * 10^7$ MD steps), during which a trajectory of 30000 configurations was stored for data analysis. Further on, umbrella sampling simulation results for different values of z_0 were combined using the weighted histogram analysis method (WHAM) to minimize the statistical error. A bin of 0.5 $\mathring{A}$ and convergence threshold of 0.1 were implemented in the analysis with WHAM. The final potentials of mean forces of NPs with different hydrophobicities were shifted to zero in the region far outside the membrane. In the following we will use the terms "potential of mean force" and "free energy" as synonyms for simplicity.

For the calculation of water permeability we used the effective water concentration of $\rho_W = 55$ mol/dm^3. The flux, J, of coarse grained water (events per time unit) is obtained in simulations as well as the total area of the bilayer, A, which changes due to oxidation. The

water permeation coefficient was then calculated as

$$P_W = \frac{J}{\rho_W \cdot A} \; ,$$

(1)

and is given in convenient units of $\mu m/s$.
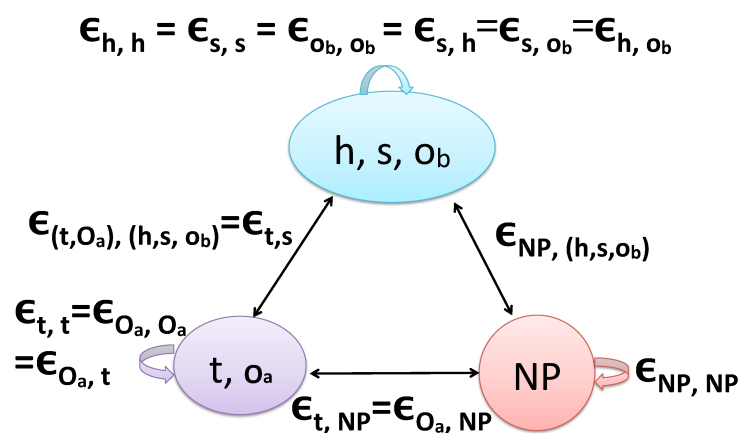
Figure 2: Scheme of the interactions used in our model. Here, h, t, s, NP, O_a and o_b represent the lipid head, tail, solvent, NP, hydrophobic and hydrophilic oxidized beads respectively. Nanoparticles can have an arbitrary degree of hydrophobicity/hydrophilicity interpolating between the extreme cases of hydrophilic (solvent-like or hydrophile) and hydrophobic (tail-like or lipophile).

The interaction sites for NPs of different degrees of hydrophobicity are illustrated in Figure 2. Regarding the hydrophobic interactions, lipid head monomers, solvent beads and hydrophilic oxidized beads o_b are identical. When the interactions of hydrophilic NPs are identical with those of solvent and lipid heads, the hydrophobicity of the NPs is defined as $H = 0$. Lipid tail monomers and hydrophobic oxidized beads O_a are indistinguishable. Hydrophobic NPs having the same interaction sites as lipid tails and hydrophobic oxidized beads are defined as $H = 1$. The effective interaction potentials between NPs of tunable

7

hydrophobicity and components in oxidized lipid bilayers are mediated as follows:

$$U_{LJ}(r) = 4\epsilon_{ij} \left[\left(\frac{\sigma_{ij}}{r} \right)^{12} - \left(\frac{\sigma_{ij}}{r} \right)^6 \right],$$

$$\sigma_{i,j} = \frac{D_i + D_j}{2},$$

$$\epsilon_{h,h} = \epsilon_{s,s} = \epsilon_{o_b,o_b} = \epsilon_{s,h} = \epsilon_{s,o_b} = \epsilon_{h,o_b} = 5 \text{ kJ/mol},$$

$$\epsilon_{t,t} = \epsilon_{O_a,O_a} = \epsilon_{O_a,t} = 3.4 \text{ kJ/mol},$$

$$\epsilon_{t,h} = \epsilon_{t,s} = \epsilon_{t,o_b} = \epsilon_{O_a,h} = \epsilon_{O_a,s} = \epsilon_{O_a,o_b} = 1.8 \text{ kJ/mol},$$

$$\epsilon_{NP,NP} = \epsilon_{s,s} + (\epsilon_{t,t} - \epsilon_{s,s}) \cdot H,$$

$$\epsilon_{NP,h} = \epsilon_{NP,s} = \epsilon_{NP,o_b} = \epsilon_{s,s} + (\epsilon_{t,s} - \epsilon_{s,s}) \cdot H,$$

$$\epsilon_{NP,t} = \epsilon_{NP,O_a} = \epsilon_{s,t} + (\epsilon_{t,t} - \epsilon_{s,t}) \cdot H.$$

$$(2)$$

This allows the hydrophobicity of NPs to be defined as follows:

$$H = \frac{\epsilon_{NP,NP} - \epsilon_{s,s}}{\epsilon_{t,t} - \epsilon_{s,s}} = \frac{\epsilon_{NP,h} - \epsilon_{s,s}}{\epsilon_{t,s} - \epsilon_{s,s}} = \frac{\epsilon_{NP,t} - \epsilon_{s,t}}{\epsilon_{t,t} - \epsilon_{s,t}}. \tag{3}$$

The precise meaning of hydrophobicity of NPs (H) can be explained by the hydrophobicity scale as discussed in Ref.[19]. The hydrophobicity scale is obtained from the free energy difference between water and oil phases for NPs of different degrees of hydrophobicity, as shown in Figure 3. The free energy difference shows a linear correlation with the hydrophobicity of NPs:

$$\frac{\Delta F}{k_B T} = 52.781 \cdot H - 24.736 = \ln(c_{\text{oil}}/c_{\text{water}}). \tag{4}$$

With this linear relationship, the parameter H of NPs can be mapped to experimental quantities, the densities of NPs in water and oil phases (c_{water}, c_{oil}). Note that for amphiphilic NPs close to $H = 0.5$, the free energy difference between two phases just vanishes. This implies that water and oil beads are indistinguishable for these NPs.
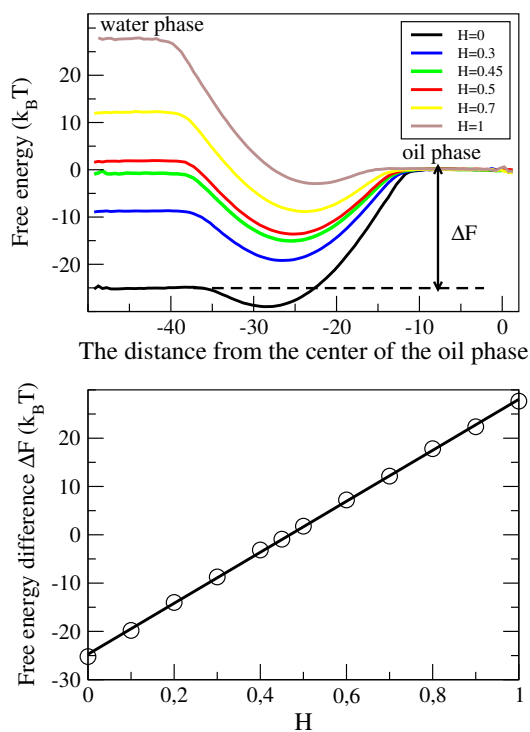
Figure 3: Upper panel: Free energy profiles of NPs as a function of the distance from the center of the oil phase. Lower panel: Free energy difference between water and oil phases for NPs as a function of NPs' hydrophobicity, H.

3   Results and Disucssions

3.1   Characterizing the oxidized lipid membranes

The introduction of hydrophilic oxidized beads in the lipid tails leads to dramatic changes in the properties of the membrane. Due to their hydrophilic character, the oxidized beads (-OOH) show a strong affinity for the lipid head groups. As a consequence, the oxidized lipid tails bend towards the hydrophilic phase. This readily explains the expansion of oxidized lipid membranes, *i.e.* the area per lipid increases significantly upon oxidation as shown in Figure 4. While the area per lipid for the non-oxidized bilayers is $61\,\text{Å}$, for the membranes OX1 and OX2, the area per lipid increases to $74.25\,\text{Å}^2$ and $76.30\,\text{Å}^2$, respectively. Such an increase obtained in our simulations is comparable to recent experimental results[10,23] and MD simulations[22] of DOPC, POPC bilayers and vesicles. Note that the increase of the area per lipid is accompanied by a decrease of the bilayer thickness from $44\,\text{Å}$ to $39.5\,\text{Å}$ due to
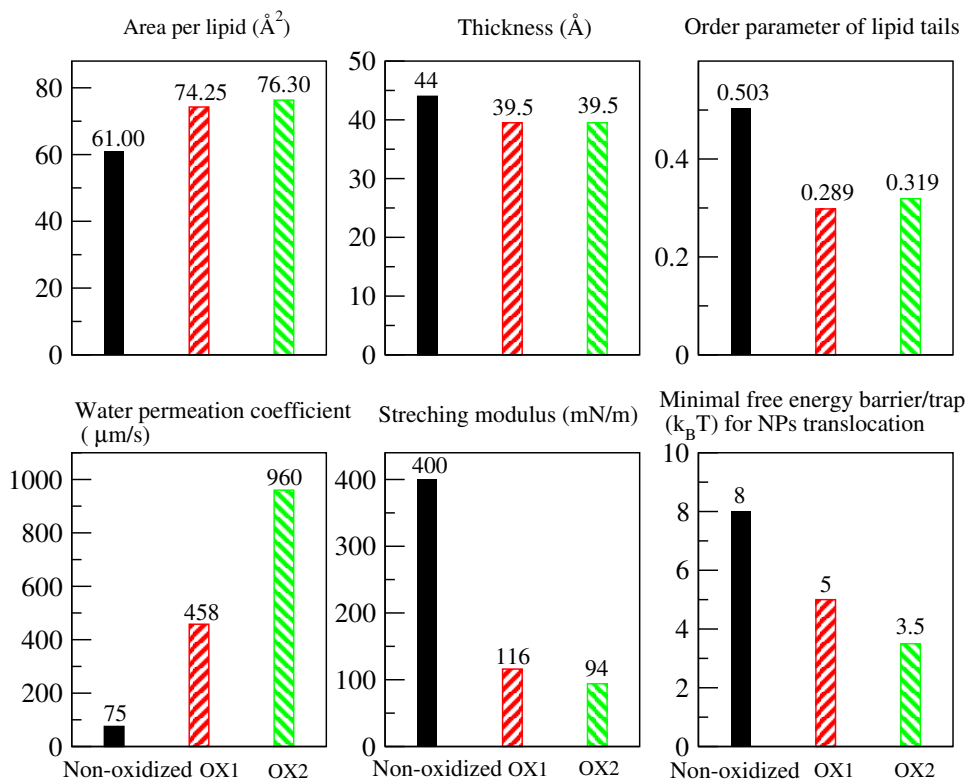
Figure 4: Comparisons of properties of non-oxidized bilayers adopted from Ref.[19] and peroxidized bilayers as obtained in present simulations. The colors correspond to non-oxidized (black), OX1 (red), and OX2 (green) membranes respectively.

peroxidation for both types of membranes, OX1 and OX2. Moreover, the order parameters of lipid tails of OX1 and OX2 decrease to 0.289 and 0.319, respectively, which are lower than in the non-oxidized bilayer (0.503). The order parameter of lipid tails was defined as follows:

$$P_2 = \langle 3\cos^2\theta - 1\rangle/2, \tag{5}$$

where θ is the angle between the end-to-end vector of each tail and the membrane's normal (z-axis). It is worth noting that the features of both membranes, OX1 and OX2, are not very different, see upper graphs in Fig. 4. Oxidation of the second tail does not lead to a significantly larger expansion of the surface area. This is due to the limited space in the head-tail interfacial region in which only a certain amount of hydrophilic oxidized beads can be accommodated. Therefore, the extra hydrophilic beads disperse in two leaflets of bilayers
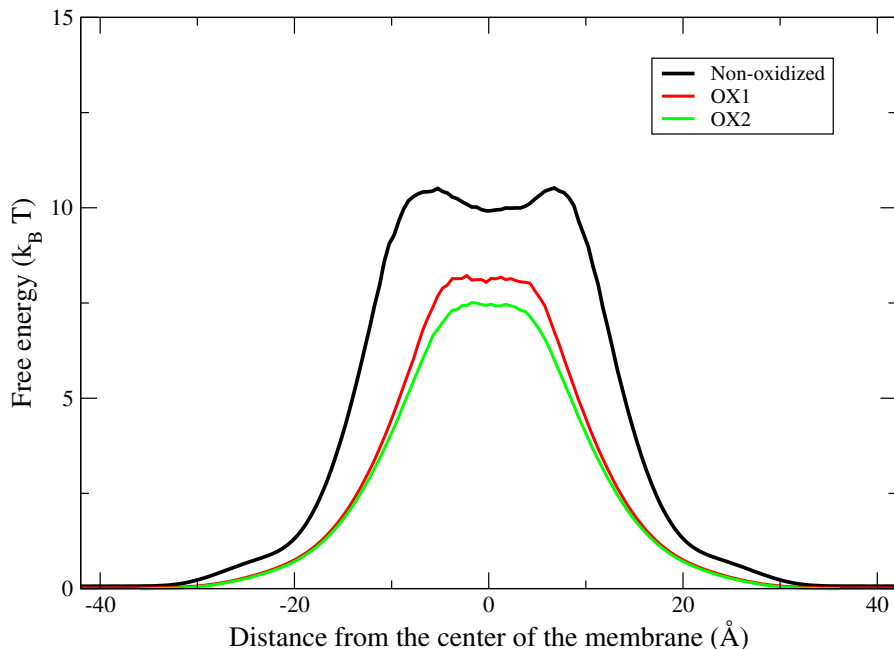
Figure 5: The free energy profiles for water translocation through the non-oxidized lipid membrane (black line), the oxidized lipid membrane OX1 (red line) and OX2 (green line). The densities of water molecules in the hydrophobic core ($-10\,\text{Å} < z < 10\,\text{Å}$), $\rho_{average}(z)$ are obtained by averaging five neighboring bins of the probability distribution to suppress the statistical noise for the non-oxidized samples. The free energy profiles for water are then obtained from this averaged probability of water: $F(z) = -k_B T \, \ln(\rho_{average}(z))$.

and do not further contribute to the surface expansion.

The water permeation coefficient as defined in Eq.(1) through the non-oxidized membrane as obtained in our previous simulations was calculated as $P_W = 75\,\mu m/s$. For the oxidized membranes OX1 and OX2 we obtained a tremendous increase to $P_W = 458\,\mu m/s$ and $P_W = 960\,\mu m/s$, respectively. A similar result has been observed in recent studies: The permeation of water is increased by one or two orders of magnitude compared to non-oxidized membranes[13,28]. Enhanced water permeation can be explained by a decrease of the free energy barriers of the bilayers, induced by the oxidation as shown in Figure 5. The free energy profiles for water beads to translocate through the bilayer are obtained from their density distribution:

$$F(z) = -k_B T \ln(\rho_{water}(z)). \tag{6}$$

A reduction of the free energy barrier has been reported in the study of the effect of lipid per-

oxidation on palmitoyl-2-linoleoyl-sn-glycero-3-phosphatidylcholine (PLPC) lipid bilayers[13]. From our simulations we show that the dramatic increase of water permeation is not related to pore formation, but rather a consequence of a reduction of the free energy barriers of the lipid bilayers, which are by nature a self-organized fluid phase. Hydrophilic oxidized beads increase the lateral distance of lipids, facilitate the penetration of water into the bilayer interior.

The elastic properties of oxidized membranes are examined by studying the stretching modulus K_A that is extracted from the fluctuations of the membrane surface:

$$K_A = \frac{k_B T \langle A \rangle}{\langle A^2 \rangle - \langle A \rangle^2} = \frac{k_B T}{4(\langle L_x^2 \rangle - \langle L_x \rangle^2)}, \tag{7}$$

where $A = L_x L_y$ is the area of the lipid bilayer and L_x and L_y are the lateral extensions of the simulation box. Since the barostat is coupled in x and y direction, L_x equals to L_y. The results in Figure 4 show that the stretching modulus of the oxidized membranes OX1 and OX2 drops from 400 mN m^{-1} to 116 and 94 mN m^{-1}, respectively. Such a sharp drop of the stretching modulus of oxidized bilayers is again consistent with previous studies[22].

Figure 6 depicts distributions of different species in non-oxidized and oxidized bilayers. For oxidized bilayers OX1 and OX2, a certain amount of hydrophilic oxidized beads is located even in between the two leaflets. We also observed hydrophilic head groups in the hydrophobic region of oxidized bilayers. This is the result of a certain amount of tilting lipids. Figure 6 shows that the main difference between the oxidized lipid membranes OX1 and OX2 consists of the distribution of hydrophilic oxidized beads. For OX1, hydrophilic oxidized beads prefer to stay at the lipid head-tail interface but also in the core of the membrane (red solid line in the middle panel of Figure 6). By contrast, in OX2, being oxidized on two tails, the majority of hydrophilic oxidized beads disperses in the leaflets due to the limited space in the interfacial regions.

Additional information about the conformations of oxidized lipids is found in the distri-
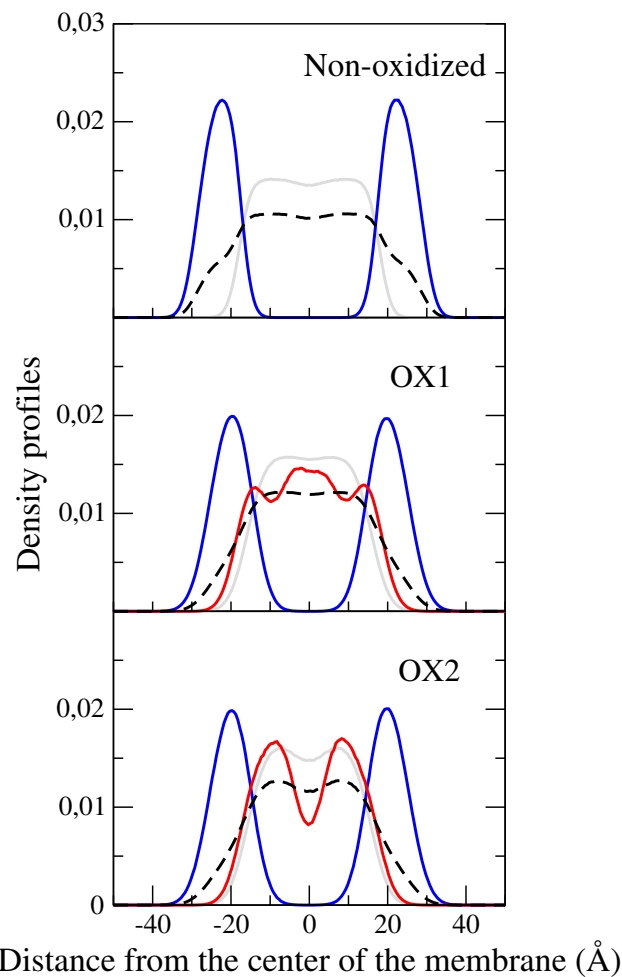
Figure 6: Normalized density profiles of different species of a non-oxidized bilayer (upper panel), lipid membranes oxidized on one tail (middle panel: OX1) and both tails (lower panel: OX2). Head group (blue solid lines), tail group (gray solid lines), hydrophilic oxidized group (red solid lines), total density of lipid molecules (black dashed lines) are presented as a function of distance from the center plane of the membrane, z.
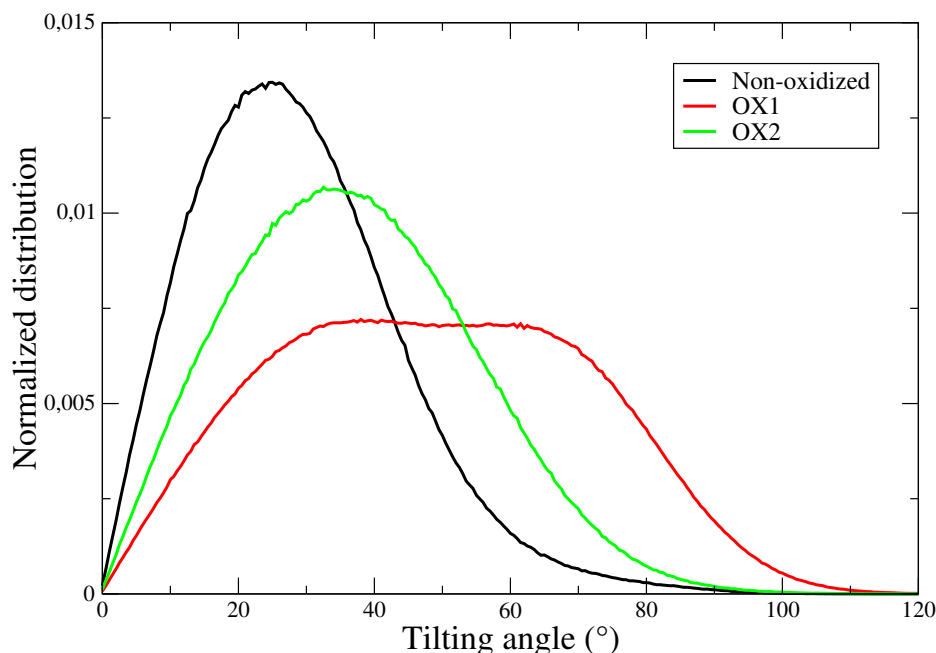
Figure 7: Distribution of tilting angles of lipid-tails for the non-oxidized bilayer (black line), the oxidized bilayers OX1 (red line) and OX2 (green line).

bution of tilting angles as shown in Figure 7. The tilting angle is defined as the angle between the direction normal to the membrane (z axis) and the vector from the hydrophobic oxidized bead (O_a in Fig.1) to the lipid head bead connected with the tails. The tilting angle of non-oxidized lipids is calculated in an analogous way considering the corresponding monomer at the place of O_a in the tails. The oxidized bilayer OX1 displays a higher occupation in the high tilting angle region. However, for the oxidized bilayer OX2, the distribution of tilting angles is narrower and displays a peak value around 34°, slightly higher compared to the non-oxidized bilayer (26°). When lipids are oxidized on only one tail, the symmetry of lipid conformation is broken, driven by the attractive interaction between hydrophilic oxidized beads and the lipid head groups.

The presence of hydrophilic oxidized groups in the tail region has an impact on the local hydrophobicity of the membrane. In Figure 8 we display the hydrophobicity profiles of the bilayers. The hydrophobicity profiles are calculated by averaging the hydrophobicity of lipid
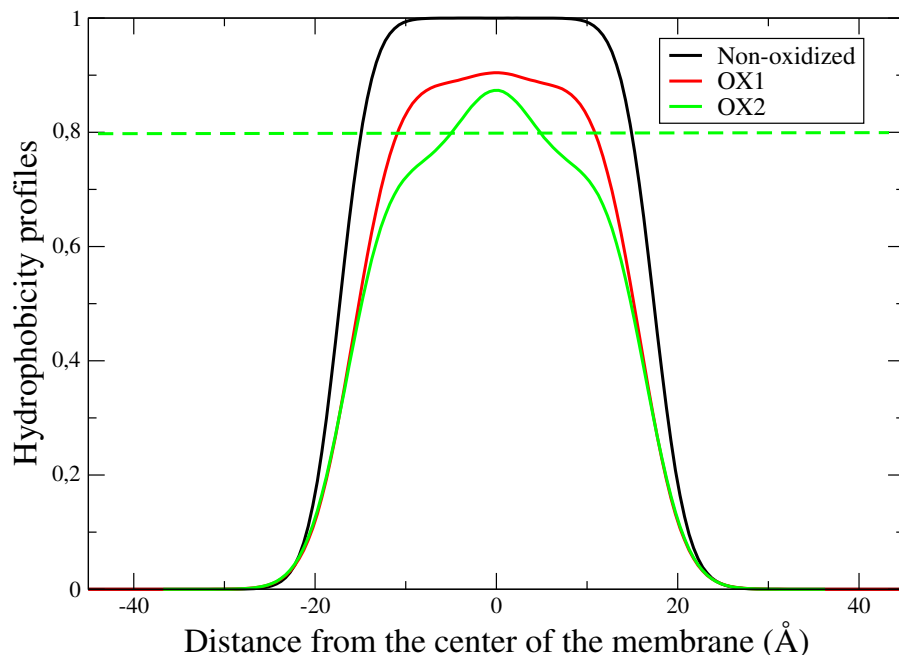
Figure 8: Hydrophobicity profiles of the non-oxidized bilayer (black line), oxidized bilayers OX1 (red line) and OX2 (green solid line). Here, the green dashed line denotes the average hydrophobicity of the core of the oxidized bilayer OX2. The core region is defined as the region between $z = z_{center} \pm 10$ Å, with z_{center} being the center of mass of the lipid membrane.

components as a function of the distance from the center of the membrane:

$$H_{average}(z) = \frac{\sum n_i(z) H_i}{\sum n_i(z)}. \tag{8}$$

Here, H_i and $n_i(z)$ denote the hydrophobicity of lipid component i and the number of lipid components at the distance (z) from the center of the membrane. The lipid components consist of the lipid head ($H = 0$), the lipid tail ($H = 1$), the hydrophobic oxidized bead ($H = 1$) and the hydrophilic oxidized bead ($H = 0$), see Figure 1. Upon oxidation, a drop of 10% and 20% of the average hydrophobicity H in the core of the oxidized bilayers is observed for the oxidized bilayer OX1 and OX2, respectively. The core of OX2 ($H = 0.8$) is more hydrophilic than OX1 ($H = 0.9$) due to the fact that more hydrophilic oxidized monomers disperse in the bilayers. This fact is of high relevance for the discussion of NP translocation through the bilayers, as described below.

3.2 Oxidized lipid membranes interacting with NPs of various degrees of hydrophobicity

As discussed in Sec. 3.1, the oxidation of the lipid tails induces significant changes of the membrane properties: the area per lipid increases, with subsequent decrease of membrane thickness. The stretching modulus of oxidized membranes drops, whereas membrane permeability for water increases dramatically. Most importantly, also the average hydrophobicity is decreased for peroxidized bilayers. The question then arises about how the interplay between NPs and oxidized bilayers is affected by these changes. Our model of the NPs is described in detail in our previous work[19] and the setup of simulation parameters and the meaning of the hydrophobicity scale is given in section Details of the Simulation Method. Let us briefly repeat the essential properties: The NP diameter is $1\,nm$, about twice as that of the coarse grained lipid beads. The hydrophobicity is controlled by the choice of the local interactions of the NPs with the other coarse grained species in the system, and can be directly mapped to an experimentally accessible value via the partition across a water/oil interface, see section Details of the Simulation Method. The membrane is kept at zero-tension and tension is also controlled in the presence of NPs. This is important since tension applied to the membrane can give rise to spontaneous pore formation, or to meta-stable pores which might be nucleated in the presence of NPs[29]. Our setup should prevent such effects, moreover, pore-opening would be monitored during the simulations.

Figure 9 shows the distributions of NPs in the oxidized membranes OX1 and OX2. It is observed that both OX1 and OX2 change from being potential barriers to being traps for NPs with increasing hydrophobicity from $H = 0$ to $H = 1$. This is consistent with the function of non-oxidized bilayers. It may be noted that the trimodal distribution of hydrophobic NPs is less pronounced, compared with the studies of non-oxidized lipid membranes presented in Ref.[19]. However, there exists in a narrow window of hydrophobicity (data not shown for other hydrophobicities) for which such a trimodal distribution persists. For the distribution of hydrophobic NPs ($H = 1$), the partition into three populations diminishes,
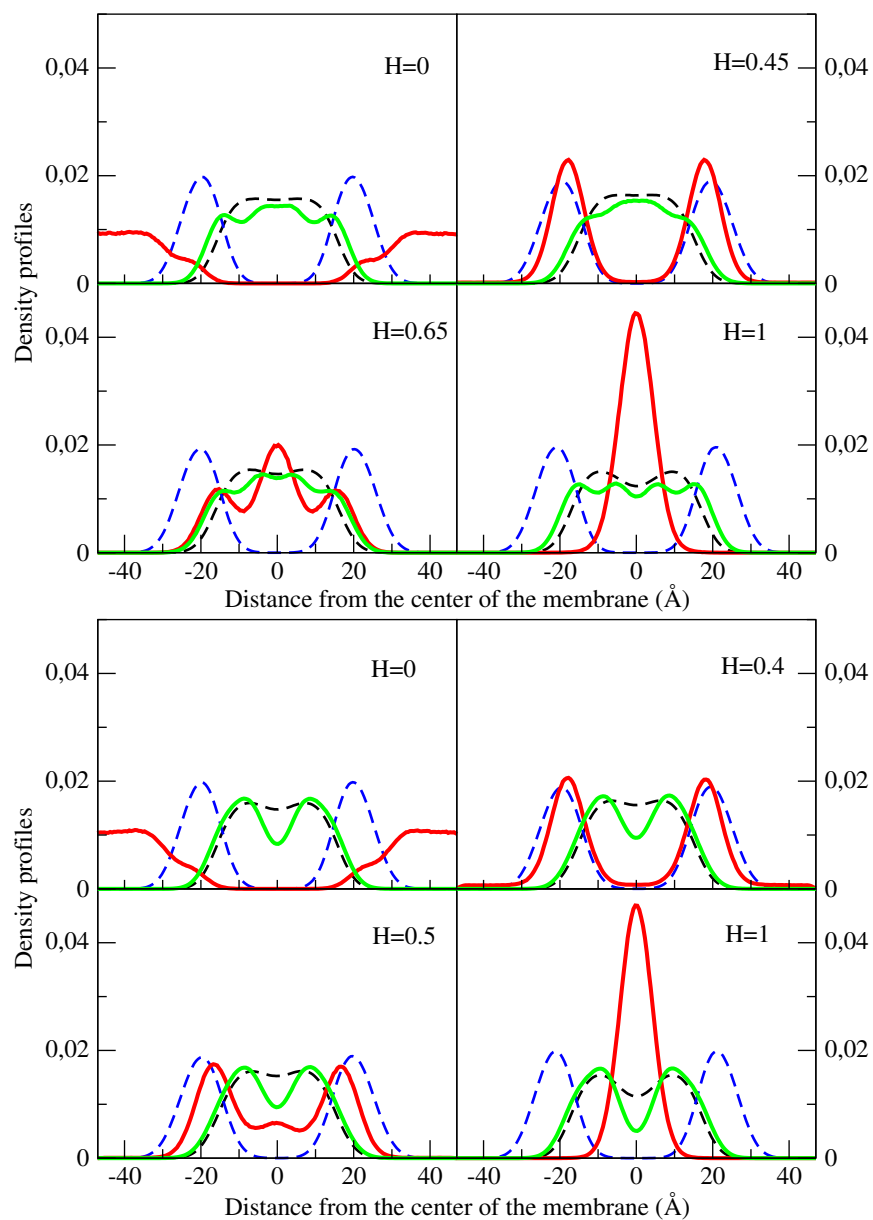
Figure 9: Density profiles of different species of oxidized bilayers OX1 (upper panel) and OX2 (lower panel) in the presence of 50 NPs of different hydrophobicity. Head group (blue dashed lines), tail group (black dashed lines), hydrophilic oxidized group (green solid lines) and NPs (red solid lines) are presented as a function of distance from the central plane of the membrane, z. The four different plots in the figure correspond to different levels of hydrophobicity, as indicated inside the plots.

i.e. the "shoulder" of the hydrophobic NP distribution at the head-tail interface vanishes. This can be understood by the fact that the oxidized membranes become softer upon oxidation, allowing hydrophobic NPs to disperse in the leaflet of oxidized membranes. Note that this absence of a three-population structure for hydrophobic NPs in the oxidized bilayers is consistent with previous studies using the bond fluctuation model (BFM) [30]. Another phenomenon that is worth mentioning is that hydrophilic oxidized beads in the oxidized bilayer OX1 accommodate to the uptake of NPs, i.e. they adjust their distribution according to the preferred location of NPs inside the membrane when the hydrophobicity of the NPs is increased.

Figure 10 (left panel) shows the translocation rates of NPs as a function of their hydrophobicity, as obtained from MD simulations. The translocation rate of NPs is calculated by counting the number of translocation events of NPs across the bilayer during the simulation time Δt:

$$f_{MD} = \frac{n_{NP}}{\Delta t}. \tag{9}$$

A translocation event is defined as a NP entering the bilayer from the solvent phase, passing across the core of the bilayer, and finally detaching from the bilayer on the opposite side. The thresholds regarding translocation events for NPs are defined as $z \pm 40 \mathring{A}$. The pronounced peaks of NP translocation through the oxidized bilayers OX1 and OX2 are located at $H = 0.45$ and $H = 0.4$, respectively. This indicates that the characteristic point for NP translocation shifts into a region of lower hydrophobicity, compared with the non-oxidized bilayer ($H = 0.5$). We denote the point of maximum translocation simply the "critical" hydrophobicity in the following which does not refer to a critical point in the sense of a phase transition here. These shifts are directly proportional to the percentage of average hydrophobicity in the core of the bilayers upon oxidation (see Figure 8). Another interesting observation is that for oxidized bilayers the maximum translocation rate of NPs at the critical hydrophobicity increases significantly compared with the case of the non-oxidized membrane. This is triggered by the fact that oxidized bilayers tend to soften upon oxidation,
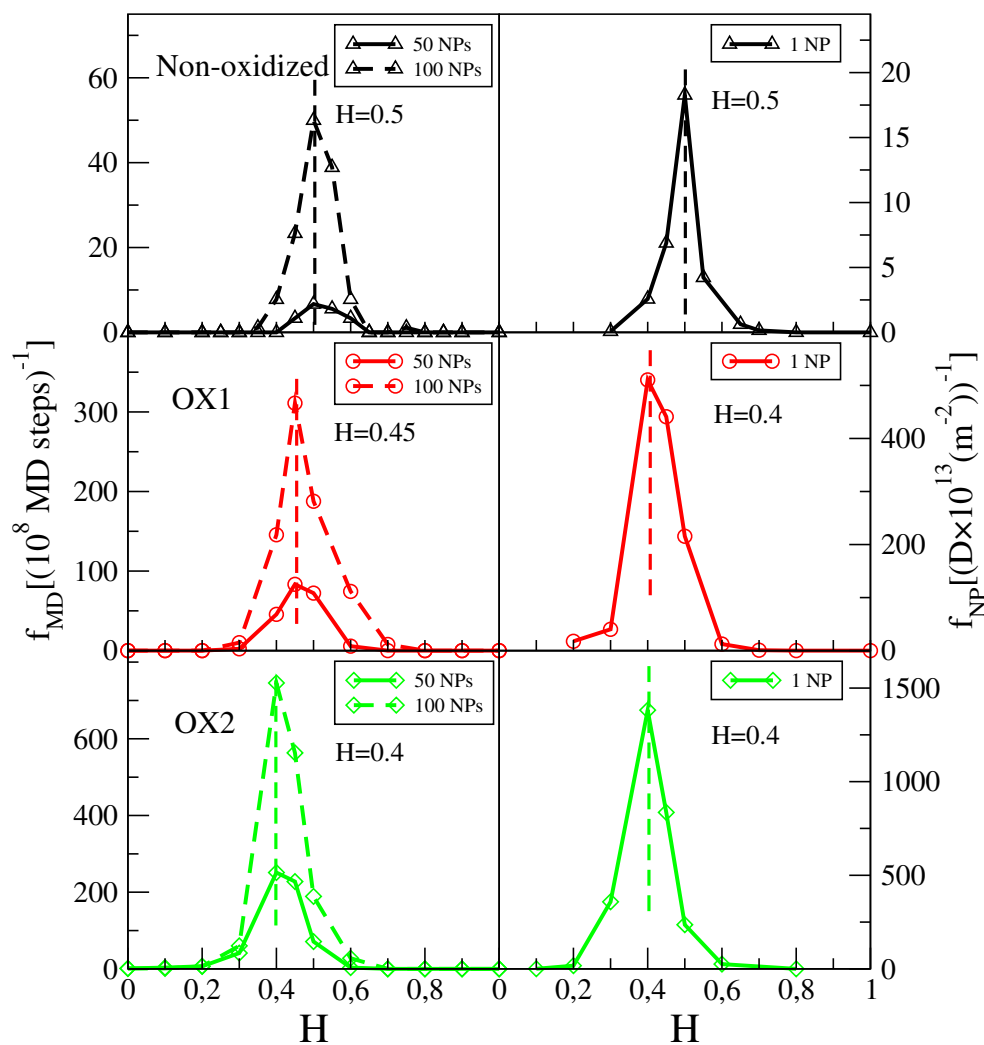
Figure 10: Frequency of translocations of NPs through the non-oxidized bilayer (upper panel, reprinted from Ref. [19]), oxidized bilayers OX1 (middle panel) and OX2 (lower panel) as a function of hydrophobicity. Left and right panels are obtained from direct MD simulations and Kramers theory, respectively.
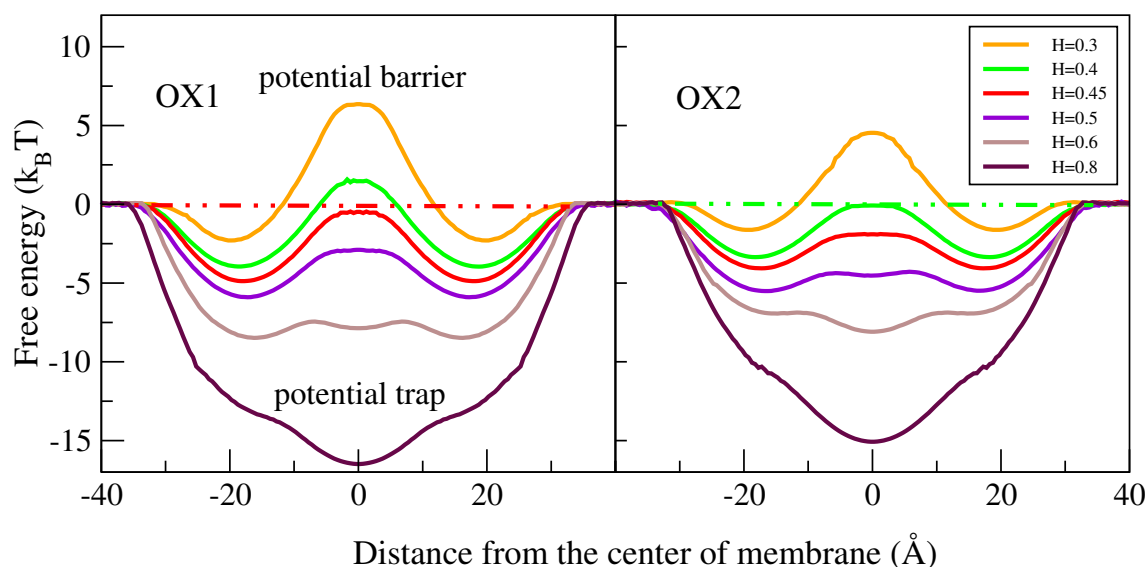
Figure 11: The free energy profiles for NPs of different hydrophobicities, translocating through the oxidized lipid membrane OX1 (left panel) and OX2 (right panel). Here, the lipid bilayer is perpendicular to the z coordinate.

accompanied with an increase of the surface area as a result of hydrophilic oxidized beads being adjacent to the tail. These findings can be verified by the following analysis of the potential of mean force presented in Figure 11. We note that the vanishing translocation rate at $H \rightarrow 1$ is the consequence of trapping nanoparticles in the membrane core, see Fig. 9, while for $H \rightarrow 0$ particles avoid the contact with the membrane. Thus hydrophobic particles impact the membrane behavior in contrast to the case of hydrophilic particles.

For oxidized bilayers interacting with NPs at the critical hydrophobicity, we can directly obtain the potential of mean force from the density distribution of NPs according to Eq. 6. This yields a lowest free energy difference of about 5 k_BT for NPs with $H = 0.45$ during a translocation through the oxidized bilayer OX1 (left panel of Figure 11), and 3.5 k_BT at $H = 0.4$ for the oxidized bilayer OX2 (right panel of Figure 11). This finding is also summarized in Figure 4. Compared with the non-oxidized membrane, the oxidized membrane imposes a lower free energy barrier for NPs translocating through the bilayer. As a consequence, translocation rates of NPs through oxidized membranes increase significantly, which explains why NPs translocating through biological membranes benefit from lipid oxidation.

For rather hydrophilic/hydrophobic NPs, it is infeasible to obtain sufficient data for all coordinates during direct MD simulations. Therefore, umbrella sampling[31] is used whenever the statistics obtained from direct sampling is not sufficient. Then, the umbrella sampling results are combined with the direct MD simulation results in order to obtain the free energy profile over the entire range. For details we refer the reader to Ref.[19]. The results are shown in Figure 11. For NPs at the critical hydrophobicity ($H = 0.45$ for OX1, $H = 0.4$ for OX2), the free energy profiles are essentially flat. This corresponds to the observation of maximal NP translocation rates as obtained from direct MD simulations (see Figure 10). Note that the free energy profiles for NPs during a translocation through the oxidized bilayers OX1 and OX2 are similar, though OX2 presents a slightly flatter and narrower barrier/trap. The smooth combination and overlap of data from direct sampling results and from umbrella sampling shows that systematic deviations due to perturbations of the membrane under the bias potential cannot be detected in our simulations. Strong deformations due to the interactions of larger NPs with lipid bilayers have been reported in earlier works[32,33], which can give rise to deviations from direct observations. The combination of direct sampling and umbrella sampling is therefore essential.

With these free energy profiles, we further calculate the mean first-passage time τ by applying Kramers theory[34,35], for the passive translocation of a NP through the oxidized bilayers OX1 and OX2:

$$\tau = \frac{1}{D} \int_{z_-}^{z_+} e^{F(z')/k_B T} dz' \int_{z_-}^{z'} e^{-F(z'')/k_B T} dz''. \tag{10}$$

Here, z_+ and z_- denote the locations of translocation of NPs, which are chosen as $z_{center} \pm 40$ Å. The diffusion coefficient D of the NP is assumed to be constant inside the membrane. The same boundaries are chosen for the calculation of translocation events of NPs from direct simulations. The translocation rate f_{NP} can further be calculated from the inverse of

the mean first-passage time τ:

$$f_{NP} = \frac{1}{\tau}. \tag{11}$$

As shown in right panel of Figure 10, the results of the translocation rate f_{NP} show a good qualitative agreement with the direct MD simulations f_{MD}, which also justifies the assumption of a constant diffusion coefficient for NPs inside the membrane. Consistent with the calculation the translocation rate is calculated for a single particle and given in units of the diffusion coefficient of the particle.

For the oxidized bilayers, a considerable enhancement of membrane permeability for water is found for NPs of hydrophobicity between $H = 0.4$ and $H = 0.8$. Hydrophobic NPs with $H = 1$ can still affect the membrane permeability because particles are trapped in the membrane in this case, see Fig. 9, contrary to the case of $H = 0$. A correlation between the membrane permeability for solvent and the area per lipid persists for the oxidized bilayers. Here, the membrane permeability for solvent is calculated by the same method as defined in Eq. 9. The results of membrane permeability for solvent of OX1 and OX2 as shown in the upper panel of Figure 12, in the presence of 50 and 100 NPs of various hydrophobicity (corresponding ratios of NPs to lipids: 1:9 and 2:9), are scaled with the results in the absence of NPs, respectively.

We characterize the membrane perturbation by the order parameter P_2 as defined in Eq. 5, as a function of the NPs' hydrophobicity. A minimum in the orientation order parameter around the critical hydrophobicity is displayed in the lower panel of Figure 12, indicating a maximum membrane perturbation induced by the uptake of NPs. In terms of the membrane perturbation and membrane permeability for solvent induced by NPs, the oxidized bilayers OX1 and OX2 display a behavior that is qualitatively similar to the non-oxidized bilayer.

It is worth noting that the rate of translocation of nanoparticles is not simply proportional to the number of particles in the system (concentration of particles), see lhs in Fig. 10. A cooperative increase of rate is most pronounced for the non-oxidized membranes and has been discussed in Ref.[19]. The reason for this is a clustering of particles for balanced
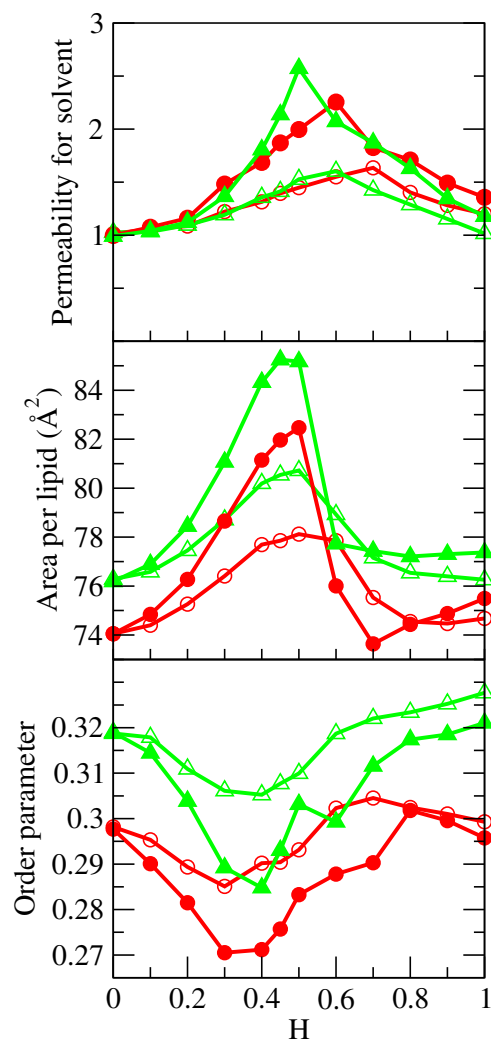
Figure 12: Dimensionless relative water permeability (upper panel) as compared with membrane in absence of NPs, the area per lipid (middle panel), and the order parameter of lipid tails (lower panel) in the presence of 50 (open symbols) and 100 (solid symbols) NPs respectively, as a function of hydrophobicity H of the particles. Here, red lines (circular symbols) and green lines (triangular symbols) denote the results for the oxidized bilayer OX1 and OX2, respectively.

values of hydrophobicity near $H = 0.5$, since here both solvent and lipid tails act as a moderately poor solvent. For the non-oxidized membrane even bridges of particles through the membrane can be temporally formed at higher concentration of nanoparticles. With increasing peroxidation this effect is reduced. One of the reasons for the lower cooperative behavior is the fact that the free energy barrier is much lower at the translocation window. This decreases the cohesiveness of the particles which are engulfed into the membrane.

4   Conclusions

We have studied the influence of peroxidation of lipids, with the focus on transport properties across the bilayer and their interactions with NPs of various degrees of hydrophobicity. In our study the nanoparticles' hydrophobicity is considered as a surface property for simplicity. A variation of the hydrophobicity of nanoparticles in experiments can be achieved by modifying or coating the particle surface in various ways such as by grafting short oligomers of different hydrophobicity. Alternatively, grafting weak polyelectrolytes which can change their effective hydrophilic behavior under variation of the pH-value of the environment is a possible way to tune the effective hydrophobicity of the particles. Two types of peroxidized lipid molecules are considered in this study, which feature hydrophilic oxidized beads on one tail only or both tails. Oxidation reactions induced by the addition of the hydrophilic polar beads to the tails lead to an expansion of the surface area, accompanied with the decrease of membrane thickness and a dramatic drop of the stretching modulus. The membrane permeability for solvent increases significantly upon peroxidation. These observations are related exclusively to the change in the free energy profile of the membrane with respect to water due to the peroxidation effect. We note that pore formation in membranes due to peroxidation and exposure to nanoparticles has not been observed in any of our simulations. A pore can be defined as a stable or transient channel through the bilayer. Instead nanoparticles are taken-up by the membrane and are fully engulfed during translocation in our simulations, see also

the snapshot on the lhs of Fig. 13. This is in perfect agreement with the potential model of

the bilayer which forms a self-organized liquid state instead of hard boundary with respect to

the environment. In our previous work we have shown analytically that a generic potential

model of the bilayer can explain corresponding results for the translocation of polymers[36].

On the other hand formation of pores in fluid membranes needs a penalty for the closed

state such as an external stress acting on the membrane[29]. The patches of our membrane

are too small to observe strong capillary waves.
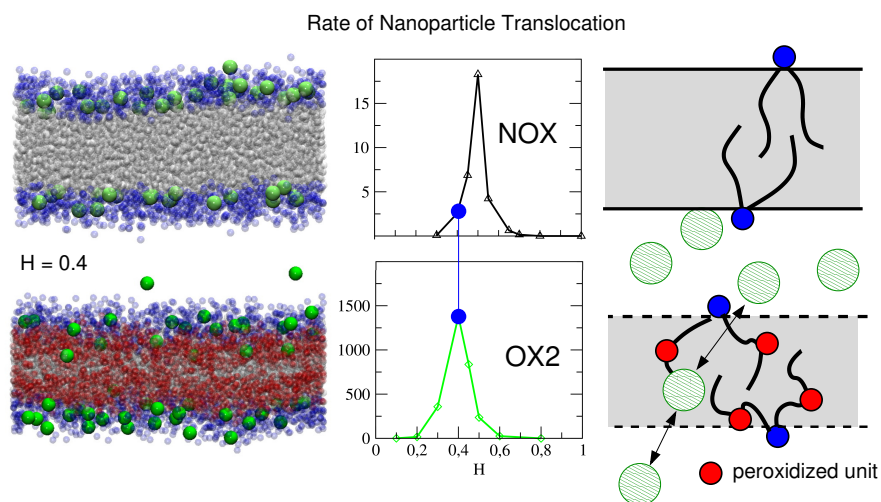
Figure 13: Illustration of the selectivity of peroxidized lipid membranes with respect to nanoparticle translocation as obtained in our simulations. The optimal setup is achieved for slightly hydrophilic nanoparticles at $H = 0.4$ and fully peroxidized lipids as given in our model study for sample OX2. In this case the relative permeability is raised by a factor of up to about 600 which opens the possibility to target peroxidized membranes by nanoparticles. The left hand side are snapshots taken from the simulations. The result for the rate of translocations are taken from Fig. 10.

The interactions between the oxidized bilayers and NPs of various degrees of hydropho-

bicity have been studied in detail. The potential model for the oxidized bilayers, which has

been discussed in Ref[19], remains valid. It is therefore consistent with previous findings for

non-oxidized bilayers. As has been observed before with non-oxidized bilayers, the translo-

cation of nanoparticles is restricted to a small window of surface hydrophobicity of particles

for which the hydrophobicity scale is in between hydrophilic and amphiphilic. However,

upon peroxidation the location of the maximum translocation rate of NPs shifts towards the

hydrophilic side. This shift is in proportion to the decrease of the average hydrophobicity in the core of oxidized bilayers. In addition, the translocation rate of NPs at the critical hydrophobicity increases significantly as compared to the case of non-oxidized bilayers, by up to an order of magnitude. This result has been confirmed by the study of free energy landscapes of NP translocation through bilayers, in which the presence of oxidized beads reduces the free energy barrier to about 5 $k_B T$ and 3.5 $k_B T$, for the oxidized bilayers OX1 and OX2, respectively. This can be potentially used to target peroxidized membranes with NPs. If the NP hydrophobicity is tuned to the maximum translocation window of the fully peroxidized membranes, see Fig. 10, located at $H = 0.4$ in our scale, the translocation rate for the same particles is two to three orders of magnitude lower, depending of the bulk concentration of NPs, for non-oxidized membranes. This huge difference is also related with the shift in the optimal hydrophobicity due to peroxidation. This shift is large enough to almost leave the translocation window of the non-oxidized membranes at the point of maximum translocation for the peroxidized membrane. This is illustrated in the middle part of Fig. 13 by the blue circles. One can see that the shift of the window increases the relative rate of translocation for the peroxidized membrane by an additional factor of about 5. Our study thus provides a possible strategy to promote the delivery of NPs to cells through the oxidation effect, thereby giving insight into the NPs' toxicity to the oxidized bilayers.

5   Acknowledgments

References

(1) Alberts, B.; Jonhson, A.; Lewis, J.; Raff, M.; Roberts, K.; Walter, P. *Molecular Biology of the Cell*, 4th ed.; Garland Science, Taylor and Francis, 2002.

(2) Reis, A.; Spickett, C. M. Chemistry of phospholipid oxidation. *BBA-Biomembranes* **2012**, *1818*, 2374–2387.

(3) Repetto, M.; Semprine, J.; Boveris, A. In *Lipid Peroxidation*; Catala, A., Ed.; IntechOpen: Rijeka, 2012; Chapter 1.

(4) Hensley, K.; Robinson, K. A.; Gabbita, S. P.; Salsman, S.; Floyd, R. A. Reactive oxygen species, cell signaling, and cell injury. *Free Radic. Biol. Med.* **2000**, *28*, 1456–1462.

(5) Mecocci, P.; MacGarvey, U.; Beal, M. F. Oxidative damage to mitochondrial DNA is increased in Alzheimer's disease. *Ann. Neurol.* **1994**, *36*, 747–751.

(6) Allan Butterfield, D. Amyloid β-peptide (1-42)-induced oxidative stress and neurotoxicity: implications for neurodegeneration in Alzheimer's disease brain. A review. *Free Radic. Res.* **2002**, *36*, 1307–1313.

(7) Ayuyan, A. G.; Cohen, F. S. Lipid peroxides promote large rafts: effects of excitation of probes in fluorescence microscopy and electrochemical reactions during vesicle formation. *Biophys. J.* **2006**, *91*, 2172–2183.

(8) Bacellar, I.; T.M. Tsubone, T.; Pavani, C.; Baptista, M. Photodynamic efficiency: from molecular photochemistry to cell death. *Int. J. Mol. Sci.* **2015**, *16*, 20523–20559.

(9) Borst, J. W.; Visser, N. V.; Kouptsova, O.; Visser, A. J. Oxidation of unsaturated phospholipids in membrane bilayer mixtures is accompanied by membrane fluidity changes. *BBA - Mol. Cell Biol. Lipids* **2000**, *1487*, 61–73.

(10) Weber, G.; Charitat, T.; Baptista, M. S.; Uchoa, A. F.; Pavani, C.; Junqueira, H. C.; Guo, Y.; Baulin, V. A.; Itri, R.; Marques, C. M.; Schroder, A. P. Lipid oxidation induces structural changes in biomimetic membranes. *Soft Matter* **2014**, *10*, 4241–4247.

(11) Aoki, P. H. B.; Schroder, A. P.; Constantino, C. J. L.; Marques, C. M. Bioadhesive giant vesicles for monitoring hydroperoxidation in lipid membranes. *Soft Matter* **2015**, *11*, 5995–5998.

(12) Rosa, R. D.; Spinozzi, F.; Itri, R. Hydroperoxide and carboxyl groups preferential location in oxidized biomembranes experimentally determined by small angle X-ray scattering: Implications in membrane structure. *BBA-Biomembranes* **2018**, *1860*, 2299 – 2307.

(13) Wong-Ekkabut, J.; Xu, Z.; Triampo, W.; Tang, I.-M.; Tieleman, D. P.; Monticelli, L. Effect of lipid peroxidation on the properties of lipid bilayers: a molecular dynamics study. *Biophys. J.* **2007**, *93*, 4225–4236.

(14) Rems, L.; Viano, M.; Kasimova, M. A.; Miklavčič, D.; Tarek, M. The contribution of lipid peroxidation to membrane permeability in electropermeabilization: A molecular dynamics study. *Bioelectrochemistry* **2019**, *125*, 46 – 57.

(15) Verma, A.; Usun, O.; Hu, Y.; Han, H.-S.; Watson, N.; Chen, S.; Irvine, D.; Stellacci, F. Surface-structure-regulated cell-membrane penetration by monolayer-protected nanoparticles. *Nat. Mater.* **2008**, *7*, 585–595.

(16) Sommer, J.-U.; Werner, M.; Baulin, V. A. Critical adsorption controls translocation of polymer chains through lipid bilayers and permeation of solvent. *Europhys. Lett.* **2012**, *98*, 18003.

(17) Werner, M.; Sommer, J.-U.; Baulin, V. A. Homo-polymers with balanced hydrophobicity translocate through lipid bilayers and enhance local solvent permeability. *Soft Matter* **2012**, *8*, 11714–11722.

(18) Werner, M.; Sommer, J.-U. Translocation and induced permeability of random am-
phiphilic copolymers interacting with lipid bilayer membranes. *Biomacromolecules*
2014, *16*, 125–135.

(19) Su, C.-F.; Merlitz, H.; Rabbel, H.; Sommer, J.-U. Nanoparticles of various degrees
of hydrophobicity interacting with lipid membranes. *J. Phys. Chem. Lett.* **2017**, *8*,
4069–4076.

(20) Marrink, S. J.; De Vries, A. H.; Mark, A. E. Coarse grained model for semiquantitative
lipid simulations. *J. Phys. Chem. B* **2004**, *108*, 750–760.

(21) Marrink, S. J.; Risselada, H. J.; Yefimov, S.; Tieleman, D. P.; de Vries, A. H. The MAR-
TINI force field: coarse grained model for biomolecular simulations. *J. Phys. Chem. B*
2007, *111*, 7812–7824, PMID: 17569554.

(22) Guo, Y.; Baulin, V. A.; Thalmann, F. Peroxidised phospholipid bilayers: insight from
coarse-grained molecular dynamics simulations. *Soft Matter* **2016**, *12*, 263–271.

(23) Aoki, P.; Schroder, A.; Constantino, C.; Marques, C. Bioadhesive giant vesicles for
monitoring hydroperoxidation in lipid membranes. *Soft Matter* **2015**, *11*, 5995–5998.

(24) Plimpton, S. Fast parallel algorithms for short-range molecular dynamics. *J. Comp.
Phys.* **1995**, *117*, 1, http://lammps.sandia.gov/.

(25) Martyna, G. J.; Tobias, D. J.; Klein, M. L. Constant pressure molecular dynamics
algorithms. *J. Chem. Phys.* **1994**, *101*, 4177–4189.

(26) Torrie, G. M.; Valleau, J. P. Nonphysical sampling distributions in Monte Carlo free-
energy estimation: Umbrella sampling. *J. Comput. Phys.* **1977**, *23*, 187–199.

(27) Kästner, J. Umbrella sampling. *WIREs Comput. Mol. Sci.* **2011**, *1*, 932–942.

(28) Lis, M.; Wizert, A.; Przybylo, M.; Langner, M.; Swiatek, J.; Jungwirth, P.; Cwiklik, L. The effect of lipid oxidation on the water permeability of phospholipids bilayers. *Phys. Chem. Chem. Phys.* **2011**, *13*, 17555–17563.

(29) Checkervarty, A.; Werner, M.; Sommer, J.-U. Formation and stabilization of pores in bilayer membranes by peptide-like amphiphilic polymers. *Soft Matter* **2018**, *14*, 2526–2534.

(30) Pogodin, S.; Werner, M.; Sommer, J.-U.; Baulin, V. A. Nanoparticle-induced permeability of lipid membranes. *ACS Nano* **2012**, *6*, 10555–10561.

(31) Binder, K.; D.W., H. *Monte Carlo Simulation in Statistical Physics*; Springer Verlag, 2010.

(32) Kopelevich, D. One-dimensional potential of mean force underestimates activation barrier for transport across flexible lipid membranes. *J. Chem. Phys.* **2013**, *139*, 134906.

(33) Neal, C.; Pome, R. Sampling errors in free energy simulations of small molecules in lipid bilayers. *Biochim. Biophys. Acta* **2016**, *1858*, 2539–2548.

(34) Schulten, K.; Schulten, Z.; Szabo, A. Dynamics of reactions involving diffusive barrier crossing. *J. Chem. Phys.* **1981**, *74*, 4426–4432.

(35) Hänggi, P.; Talkner, P.; Borkovec, M. Reaction-rate theory: Fifty years after Kramers. *Rev. Mod. Phys.* **1990**, *62*, 251.

(36) Werner, M.; Bathmann, J.; Baulin, V.; Sommer, J.-U. Thermal tunneling of homopolymers through amphiphilic membranes. *ACS Macro Lett.* **2017**, *6*, 247–251.

TOC Graphic